Microphysical modelling of a midlatitude "polar stratospheric cloud" event: Comparisons against multiwavelength ground-based and spaceborne lidar data

Julien Jumelet, Slimane Bekki, Patric Seifert, Nadège Montoux, Jean-Paul Vernier, Jacques Pelon

Microphysical modeling of a midlatitude "polar stratospheric cloud" event: Comparisons against multiwavelength ground-based and spaceborne lidar data

Julien Jumelet,[1] Slimane Bekki,[1] Patric Seifert,[2] Nadège Montoux,[1] Jean-Paul Vernier,[1] and Jacques Pelon[1]

[1]   A high-resolution transport model containing a fully explicit size-resolving microphysical scheme is used to study a large-scale polar stratospheric cloud (PSC) case detected by lidar at midlatitudes between 17 and 23 February 2008. The model simulations, initialized using European Centre for Medium-Range Weather Forecasts (ECMWF) fields and Microwave Limb Sounder (MLS) Aura data, are validated locally against ground-based (Institute for Tropospheric Research Multiwavelength Atmospheric Raman lidar for Temperature, Humidity, and Aerosol profiling (IfT MARTHA)) lidar measurements at Leipzig and globally against spaceborne (Cloud-Aerosol LIdar with Orthogonal Polarization/Cloud-Aerosol-Lidar and Infrared Pathfinder Satellite Observations (CALIOP/CALIPSO)) lidar backscatter measurements. By assuming a 1 K cold bias on the ECMWF temperatures and under the assumption of equilibrated spherical PSC particles, our model produces fields of optical and microphysical parameters like the total surface area density (A) and volume (V). A, and V, as well as the median radius of the PSC size distribution, compare favorably to the corresponding values derived from multiwavelength lidar backscatter measurements. Around 21 km, A and V are found to be around 10 μm^2 cm^{-3} and 1 μm^3 cm^{-3}, respectively. The median radius of the Supercooled Ternary Solution particle size distribution is estimated to be around 0.3 μm using both the model calculations and the lidar-derived size distribution parameters. Overall, despite the simplifications on the microphysical scheme, the model is able to reproduce the salient features of the local and global lidar observations. The results clearly demonstrate the value of CALIOP products for large-scale studies, exploiting chemistry-transport models.

1.   Introduction

[2]   Polar stratospheric clouds (PSCs) usually form in the polar lower stratosphere in winter at low temperatures. They have been investigated over 2 decades and the dual role of these clouds in polar ozone depletion is now well established [*Solomon*, 1999; *WMO*, 2007]. First, PSC particles provide reactive surfaces for heterogeneous chemical reactions that convert stable halogen reservoir species into highly reactive ozone-destroying radicals. Second, by sedimenting, large PSC particles cause an irreversible downward transport of nitric acid and, hence, a partial removal of reactive nitrogen from the altitudes of PSC-induced ozone depletion, the so-called denitrification phenomenon. This, in turn, extends the lifetime of reactive halogen radicals, favoring further polar ozone destruction.

[3]   PSCs have been characterized using a range of ground-based, airborne and spaceborne instruments. Different types of PSCs have been identified: liquid HNO_3-rich clouds (type Ib PSCs) [*Tabazadeh et al.*, 1994; *Carslaw et al.*, 1994; *Weisser et al.*, 2006], solid HNO_3-rich clouds (type Ia PSCs) [*Larsen et al.*, 2004] and ice clouds (type II PSCs) [*Goodman et al.*, 1989; *Toon et al.*, 1990]. When the temperature reaches about 195 K, solid HNO_3-rich clouds can form on the preexisting supercooled sulphuric acid (H_2SO_4-H_2O) aerosols; solid HNO_3-rich clouds are composed of solid particles of Nitric Acid Trihydrate (NAT). However, owing to energy barriers associated with the NAT crystal formation from liquid binary H_2SO_4-H_2O solution, NAT PSCs often do not form as soon as the NAT temperature threshold (T_{NAT}) is reached. In that case, at several K below T_{NAT}, H_2SO_4-H_2O aerosols experience a sharp growth by uptake of gaseous HNO_3, forming liquid

---

[1]Service d'Aéronomie, IPSL, UPMC, CNRS, Paris, France.
[2]Leibniz Institute for Tropospheric Research, Leipzig, Germany.

HNO$_3$-rich clouds composed of supercooled liquid ternary (H$_2$SO$_4$-HNO$_3$-H$_2$O) solution; these clouds are either called STS (Supercooled Ternary Solution) or LTA (Liquid Ternary Aerosols) PSCs. When the temperature drops to the ice temperature threshold T$_{ICE}$ (near 190 K), large ice particles may form, probably on the top of NAT PSCs [*Poole and McCormick*, 1988; *Voigt et al.*, 2000, 2005].

[4] Because of their high vertical resolution and high sensitivity to aerosols and clouds, lidar (light detection and ranging) observations have been the most extensively used data sets for PSC studies and model validation [*Hansen and Hoppe*, 1997; *Mehrtens et al.*, 1999; *Brooks et al.*, 2004; *Blum et al.*, 2006; *Jumelet et al.*, 2008a, 2008b]. They have helped in investigating PSC formation processes and composition. Local PSC climatologies were also established from lidar data through continuous monitoring and measurement campaigns [*Browell et al.*, 1990; *David et al.*, 1998; *Biele et al.*, 2001; *Daneva and Shibata*, 2003; *Adriani et al.*, 2004; *David et al.*, 2005; *WMO*, 2006, 2007]. There still exist issues when only using lidar data, the spatial sampling of the atmosphere being the major one. Ground-based lidar systems only probe a very narrow air column above the measurement stations. Airborne lidar sampling, often carried out during measurement campaigns, remains very sparse both in space and time. Moreover, although aircraft can follow moving air masses, Lagrangian flight paths remain difficult to achieve. Satellite measurements provide a much better spatiotemporal sampling, with continuous measurements often performed on a quasi-global coverage. Until recently, large-scale distributions of PSCs were derived from limb measurements such as SAGE (Stratospheric Aerosol and Gas Experiment) [*McCormick et al.*, 1979; *Polyakov et al.*, 2008], SAM (Stratospheric Aerosol Measurement) [*Poole and Pitts*, 1994] and POAM data (Polar Ozone and Aerosol Measurement POAM) [*Fromm et al.*, 1997, 2003]. Unlike lidar data, the limb satellite data have a relatively poor spatial resolution, typically several kilometers vertically and a couple of hundred kilometers horizontally. This lack of resolution in satellite data has been vastly remedied by locating lidar instruments in space. The first spaceborne lidar measurements were carried out with the Lidar In-space Technology Experiment (LITE) instrument on board the American shuttle in 1993 [*Winker et al.*, 1996]. The first long-duration spaceborne lidar was the Geoscience Laser Altimeter System (GLAS) instrument on board the Ice, Cloud and land Elevation Satellite (ICESat) which launched in 2003 [*Palm et al.*, 2005; *Mueller et al.*, 2008] and is now operated intermittently. The first and only lidar instrument on a satellite is the Cloud-Aerosol LIdar with Orthogonal Polarization (CALIOP) instrument on board the Cloud-Aerosol Lidar and Infrared Pathfinder Satellite Observations (CALIPSO) satellite that was launched in 2006 to be flying in close proximity with 5 other research satellites, the so-called A-Train formation [*Winker et al.*, 2003, 2006]. Because of its high spatial resolution and polar orbit sampling, CALIOP/CALIPSO has started producing the most comprehensive data set available to date on aerosols and clouds. It should help to better characterize and parameterize PSCs in global models [*Pitts et al.*, 2007; *Noel et al.*, 2008].

[5] The region where PSC fields are the most difficult to model is the Arctic lower stratosphere [*Hendricks et al.*,

2001; *Carslaw et al.*, 2002; *Fueglistaler et al.*, 2003]. In contrast to the Southern Hemisphere, the Arctic temperatures are usually quite variable in space and time. On average, the Arctic winter temperatures tend to hover around the PSC formation temperature threshold. As a result, PSC formation is often intermittent and PSC fields are rather patchy in the Northern Hemisphere. The situation is very different in the Antarctic where the polar vortex is strong and stable with temperatures well below the PSC formation threshold. As a result, Antarctic PSCs fields are large and more or less permanent during the winter without exhibiting substantial interannual variability.

[6] As marginal conditions prevail in the Northern Hemisphere, uncertainties in the temperature make it difficult to accurately predict the evolution of PSC size and spatial distributions [*Knudsen*, 1996; *Pullen and Jones*, 1997; *Knudsen et al.*, 2002]. In the same way, accurate PSC modeling should account for air mass temperature history. Hysteresis phenomena due to kinetic barriers when forming solid particles actually occur when temperature passes through the NAT and ice thresholds (T$_{NAT}$, Tice). Typically, supersaturation (T < T$_{NAT}$-3K) is needed to form NAT, but evaporation only takes place at T$_{NAT}$. This hysteresis process is obviously not simulated in models where thermodynamic equilibrium is assumed. Most PSC schemes integrated in global models still assume thermodynamical equilibrium between the PSC (condensed) phases and the gas phase [*Lefevre et al.*, 1991; *Daerden et al.*, 2007; *Marchand et al.*, 2007]. There are now strong evidences that orographically induced PSCs (i.e., produced by gravity waves) are not in equilibrium with the gas phase [*Carslaw et al.*, 1998; *Voigt et al.*, 2000], gravity waves being much more frequent and pronounced in the Arctic than in the Antarctic. These small-scale waves are also not properly resolved in large-scale models. Moreover, there are uncertainties in thermodynamical parameters of PSC schemes such as equilibrium water vapor and nitric acid partial pressures which can lead to up to 2 K errors in transition temperatures from H$_2$SO$_4$-rich aerosols to liquid HNO$_3$-rich PSCs [*Carslaw et al.*, 1997]. Ultimately, errors in model-simulated PSC size and spatial distributions generate errors in denitrification rates (from PSC sedimentation) and production rates of ozone-destroying halogen radicals through PSC heterogeneous chemistry, two key processes for polar ozone losses. It is therefore of interest to validate PSCs simulated by large-scale models, especially in the Northern Hemisphere, with the latest generation of lidar data. This is the substance of the present work.

[7] The paper focuses on PSCs formation at northern midlatitudes, a region where detection of such clouds remains rare. PSCs can still form at midlatitudes when the polar vortex is highly distorted with filaments extending down far south and when very low temperatures are prevailing at midlatitudes. These events can result in significant direct ozone destruction, especially during the winter [*Keckhut et al.*, 2007]. It may be important to simulate these events realistically if they are to become more frequent in the future. For this reason, the present work represents a case study of such a PSC event which occurred in late February 2008. It was detected by both the Leibniz-Institute for Tropospheric Research (IfT) ground-based lidar at Leipzig (51.4°N, 12.4°E), Germany, and the

spaceborne lidar CALIOP/CALIPSO. The event is analyzed using a global aerosol-cloud microphysical transport model, MIMOSA-$\mu\varphi$. The model is able to simulate the formation, transport and some microphysical evolution of aerosols and PSC particles under the assumption of thermodynamical equilibrium. The model includes a fully explicit size-resolving microphysical module linked to an optical module able to calculate the scattering properties at lidar wavelengths, from the microphysical properties for validation purposes. The model simulations are evaluated against measured particle backscatter signals and against key particle size distribution properties (mean size, surface area and volume density) retrieved from multiwavelength lidar data [*Jumelet et al.*, 2008a]. Note that there have been few attempts at validating in detail PSCs simulated in global models [*Lefevre et al.*, 1991; *Daerden et al.*, 2007]. Most of the validation work has however been devoted to Lagrangian (trajectory) microphysical models that can be run with detailed microphysics and a low requirement in computational power [*Carslaw et al.*, 1998; *Wirth et al.*, 1999; *Larsen et al.*, 2002; *Santee et al.*, 2002; *Eckermann et al.*, 2006].

[8] The paper is organized as follows. Section 2 describes the global microphysical transport model and its setup for the comparisons with lidar data. The lidar observations and the retrieval of the particle size distribution from multiwavelength data are presented in section 3. In section 4, the midlatitude PSC event is documented using meteorological analyses, ground-based and spaceborne lidar observations. Section 5 is devoted to the model results and their comparison to lidar backscatter data. Model-simulated PSC size distributions are evaluated against the size distributions derived from lidar ground-based data in section 6. Section 7 is devoted to concluding remarks.

2. Microphysical Transport Model MIMOSA-$\mu\varphi$

2.1. MIMOSA Advection Model

[9] The Modèle Isentropique de transport Mésoéchelle de l'Ozone Stratosphérique par Advection (MIMOSA) model [*Hauchecorne et al.*, 2002] is originally a Potential Vorticity (PV) advection model running on isentropic surfaces (surfaces of constant potential temperature). The advection scheme is semi-Lagrangian with a time step of 1 h. The regridding onto the original orthonormal grid is performed every 6 h. The model resolution is $1° \times 1°$. The advection is driven by European Centre for Medium-Range Weather Forecast (ECMWF) meteorological analyses at a resolution of $2.5° \times 2.5°$. In the case of the PV, its slow diabatic evolution is taken into account by relaxing the model PV toward the PV calculated from the ECMWF fields with a relaxation time of 10 days. Using this procedure, it is possible to run the model continuously and follow the evolution of PV filaments during several months, for instance from November to April for the study of the filamentation and the breakup of the Arctic vortex. The accuracy of the model has been evaluated by *Hauchecorne et al.* [2002] and validated against airborne lidar ozone measurements using the strong correlation between PV and ozone, a quasi-conserved chemical tracer on a week time scale within most of the lower stratosphere [*Heese et al.*, 2001].

2.2. Microphysical and Optical Module

[10] The microphysical module is loosely based on a very detailed aerosol-PSC size-resolving microphysical box model which is extensively described by *Larsen* [2000] and *Larsen et al.* [2002]. The box model calculates the temporal evolution of the size distributions and chemical compositions of 4 types of particles (H_2SO_4/H_2O aerosols, STS, NAT and ice PSCs) together with the associated changes in gas phase mixing ratios of H_2O and HNO_3. It simulates the formation, growth, evaporation, and sedimentation of these four particle types. The model also describes several processes for the transitions between the different types of PSCs such as homogeneous freezing or melting. Vapor pressures over STS, NAT and ice are taken from *Luo et al.* [1995], *Hanson and Mauersberger* [1988] and *Marti and Mauersberger* [1993], respectively. In the Eulerian version of the model (in the size space), the particle size distribution is discretized into a number of size bins using a geometrically increasing volume scale because the particle sizes span several orders of magnitudes [*Turco et al.*, 1979; *Toon et al.*, 1988]. The model prognostic variables are the number density and chemical composition of each size bin for the four types of particles. Owing to computational constraints, the number of size bins is set to 20 for each of the four particle types in the present study with a particle radius of the bins ranging from 0.01 to 5 μm. Note that there are uncertainties in the optical calculations due to this limited number of bins. From sensitivity studies, this error is estimated to be around 20%, considering the PSCs detected at IfT. This needs to be kept in mind when interpreting the comparisons between the simulations and the lidar measurements.

[11] The microphysical module inserted in the MIMOSA model is greatly simplified assuming that H_2O and HNO_3 are in thermodynamical equilibrium between gas phase and condensed phases when PSCs form. The only microphysical process relevant to this study is the condensation/evaporation of H_2O and HNO_3 which is supposed to be instantaneous to maintain thermodynamical equilibrium. In order to determine the particle equilibrium composition (weight fractions in sulphuric acid, nitric acid and water vapor), one has to solve a system of two nonlinear equations describing the equality between the partial pressures of HNO_3 and H_2O just over the surface of the condensed phase and the partial pressures in the gas phase. In the end, the refractive index is calculated from the equilibrium composition assuming that STS particles are nonabsorbing.

[12] The microphysical module also includes an optical routine that calculates the particle optical properties such as volume backscatter and/or extinction coefficients at specified wavelengths (in the visible and near-infrared domains) from the model-simulated particle size distribution and the composition-dependent refractive index. For the evaluation of the model simulations against lidar observations, we only consider the backscatter ratio (hereafter called BR), defined as

$$BR_\lambda = 1 + \frac{\beta_{Par,\lambda}}{\beta_{Ray,\lambda}},$$

where β_{Par} and β_{Ray} are respectively the particular and Rayleigh backscatter coefficients at the wavelength λ.

2.3. Coupling the Particle Advection and Microphysics

[13] Gaseous H_2O and HNO_3 are advected in the model like other tracers. Sulphuric acid is assumed to be only present in the condensed phases in the model. This assumption is perfectly valid in the lower stratosphere for the time scale of the present study. The lower stratospheric aerosol depends, on the longer scale, on input of sulfur from OCS dissociation and volcanic input of SO_2.

[14] The advection of the particles is more problematic. Particles of a given size bin indeed have by essence the same size over the entire model domain, but not the same composition because of the different environmental conditions (temperature, pressure, $H_2O_{(g)}$, $HNO_{3(g)}$) in the different grid cells. As long as the composition of the particles at a given size varies over the model domain, these particles cannot be directly advected like the other tracers. The assumption of thermodynamical equilibrium gives an opportunity to bypass this issue with a numerical artifice. The model domain is initialized with H_2O/H_2SO_4 aerosols having a fixed reference composition (over 60% H_2SO_4 weight percent) which has been chosen to fit the winter lower stratospheric climatological conditions at high latitudes (T = 200 K; $H_2O_{(g)}$ = 5 ppmv; $HNO_{3(g)}$ = 10 ppbv). For these conditions, PSC formation is precluded, and consequently, all H_2O and HNO_3 molecules are supposed to be in the gas phase. As H_2O/H_2SO_4 aerosol particles are arbitrarily forced to the same composition over the entire domain, they can then be advected like a passive tracer. Therefore, an additional tracer has been added in the model for each aerosol size bin. When the size distributions and compositions of equilibrated aerosols and PSCs in a grid cell are required for microphysical and optical calculations, the thermodynamical equilibrium is simply reestablished by running the microphysical module starting from the H_2O/H_2SO_4 aerosol distribution at reference composition and then let it evolve toward equilibrium with the gas phase under the actual environmental conditions of the grid cell (ECMWF temperature, pressure and advected gaseous H_2O and HNO_3 from satellite observations). When global output fields are required, this equilibration procedure is performed in every grid cell over the whole model domain. In other words, when advection is applied to the model, particles are first adjusted to the reference composition, advected, and then adjusted back to the local equilibrium condition.

[15] We check the accuracy of such an approach by also advecting the initial total H_2O, total HNO_3 and total H_2SO_4. On a week of simulation time, no noticeable differences are found in any grid cell between the mass of a specific total tracer (H_2O, HNO_3 or H_2SO_4) and the sum of the masses of the gaseous tracer (H_2O or HNO_3) and its corresponding condensed parts (H_2O, HNO_3 or H_2SO_4 in aerosols and PSCs) before or after equilibration. And as expected, the choice of the reference composition of H_2O/H_2SO_4 aerosols has no noticeable impact on the equilibrated model results.

[16] There are still limitations to our approach. It cannot account for nonequilibrated particles, typically observed when particles experience rapid temperature variations, for instance in mountain lee waves. In such cases, the composition may depend on the particle size [*Larsen*, 2000; *Voigt et al.*, 2005]. The equilibrium assumption also prevents us from treating the kinetics of phase transitions. As a result, STS PSCs can form only if NAT PSCs are not allowed to form because the STS temperature threshold is lower than the NAT temperature threshold. Nonetheless, when necessary, both STS and NAT simulations can be performed for the same conditions.

2.4. Model Setup and Initialization

[17] To evaluate the overall quality of the model simulations of PSC geometrical and optical properties, we first have to ensure that the input data are as accurate as possible. The input variables to the microphysical module are pressure, temperature, mixing ratios of gaseous H_2O and HNO_3, and the numbers and compositions of the different particles. Obviously, only $H_2O_{(g)}$, $HNO_{3(g)}$, and the latter numbers and compositions are modified within the module. The model initialization in H_2O and HNO_3 is based on measurements of the Microwave Limb Sounder (MLS) instrument on the AURA platform [*Vomel et al.*, 2007; *Barnes et al.*, 2008]. On a weekly time scale, H_2O and HNO_3 can be considered chemical tracers in the winter lower stratosphere except in the regions affected by PSCs. They tend to exhibit relatively compact relationships with other chemical tracers [*Proffitt et al.*, 1990; *Mote et al.*, 1996; *Engel et al.*, 1996; *Irie et al.*, 2001; *Wetzel et al.*, 2002] and with dynamical tracers such as PV [*Schoeberl et al.*, 1997; *Lary et al.*, 1995]. It is possible to reconstruct isentropic fields of chemical tracers from the correlation between PV and chemical tracers' mixing ratio in the stratosphere, as described by *Lary et al.* [1995]. First, using ECMWF analyses, we determine the PV value of each MLS/AURA measurement carried out over a 3-day period centered on the starting time of the model simulation. The measurements made in regions where the temperature is less than 195 K are ignored in order to avoid the effects of PSCs on HNO_3. Second, MLS/AURA measurements are binned according to their PV values and then averaged, providing a relationship between PV and the chemical tracer mixing ratio on an isentropic surface. Finally, the model initial chemical tracer fields are reconstructed using the PV field of the starting time of the model simulation and the relationships between PV and H_2O or HNO_3 mixing ratio. These reconstructed fields provide a good estimation of the fields of total (= gaseous + condensed) H_2O and HNO_3 available because only measurements made in PSC-free regions are taken into account in this mapping-reconstruction procedure and the amount of H_2O trapped in H_2SO4/H_2O aerosols is negligible.

[18] As the aerosol levels are close to background (i.e., nonvolcanic) conditions for the period of interest, H_2O/H_2SO_4 aerosols are initialized with the same typical background size distribution (assuming a lognormal distribution with N_o = 10 cm^{-3}, r_m = 0.07 μm and σ = 1.86 [*Pinnick et al.*, 1976]) over the entire model domain. Model tests show that the model results are not sensitive to the assumed H_2O/H_2SO_4 aerosol size distribution when the values of size distribution parameters are varied within the ranges of background values [*WMO*, 2006; *Deshler et al.*, 2006].

[19] As already found in previous works, all our model tests show that temperature is actually the key factor controlling PSC formation. In order to account for biases both in ECMWF analyses that can occasionally exceed several K in some cases [*Knudsen et al.*, 2002] and in STS transition temperatures [*Carslaw et al.*, 1997], we perform several sensitivity simulations where a range of

temperature corrections is explored. We present here the three most relevant model simulations. The first simulation is run with unchanged ECMWF temperature, and will be labeled (T), whereas the two other simulations run with a uniform negative correction of 1 and 2 K on the ECMWF temperatures; these simulations will be labeled (T-1K) and (T-2K), respectively. Note that adjusting model temperatures is not at all an equivalent to the modeling of the nonequilibrium aspects of PSC formation. The simulations are evaluated against the lidar backscatter data. The validation in terms of PSC size distribution is limited to the simulation displaying the best match regarding the backscatter ratio.

[20] Each simulation is run from 1 to 23 February at multiple altitude levels to allow profile comparisons with the lidar measurements. As lidar depolarization measurements indicate that the PSCs of the February 2008 event are mostly nondepolarizing, i.e., liquid (see section 4), only liquid STS PSC simulations are run (NAT formation is not allowed). The associated optical module takes the model-simulated compositions and size distributions of the newly equilibrated aerosol and PSC particles as input and calculates the particular backscatter coefficient and backscatter ratio. The model calculates the particle composition from a binary H_2SO_4/H_2O solution to a ternary $H_2SO_4/HNO_3/H_2O$ solution [*Luo et al.*, 1996; *Krieger et al.*, 2000]. The required refractive index is calculated from the composition following *Luo et al.* [1995] fits.

3. Lidar Instrumentation and Methodology

3.1. MARTHA IfT European Aerosol Research Lidar Network Lidar

[21] The Institute for Tropospheric Research (IfT) in Leipzig has been operating the lidar system MARTHA (Multiwavelength Atmospheric Raman lidar for Temperature, Humidity, and Aerosol profiling) since 1997 [*Mattis et al.*, 2008]. The lidar setup can measure particle backscatter and extinction up to the lower stratosphere. An Nd-Yag laser emits 30-Hz-frequency laser pulses from the fundamental 1064-nm wavelength. Two optically nonlinear crystals multiply the frequency to 532 and 355 nm. The divergence of the emitted light beam is around 0.1 mrad with a 15-cm diameter. The backscattered light is detected on a 1-m-diameter Cassegrain Telescope in photon-counting mode. An extensive description of the whole signal processing chain is available from *Mattis et al.* [2002]. The instrument is equipped with filters separating the perpendicular and parallel signal components, giving access to the depolarization ratio, which complements well the multiwavelength detection capability by providing information about the shape of the scattering particles. The inelastic N_2 Raman diffusion at 387 and 607 nm is also detected. The N_2 vibrational Raman signals help in deriving the particle backscatter coefficient by providing an estimate of the particle lidar ratio (i.e., extinction to backscatter coefficients) at 355 and 532 nm, which is required in the lidar inversion algorithm [*Ansmann et al.*, 1990, 1992a, 1992b]. PSCs were detected during the night of 19 to 20 February 2008. Data are averaged on 2-h time intervals, 2344–0136 and 0136–0333 UTC, in order to maximize the signal-to-noise ratio and minimize the lidar errors, which is of importance for the size distribution retrieval [*Jumelet et al.*, 2008a].

3.2. Particle Size Distribution Retrieval From Multiwavelength Lidar Data

[22] An exhaustive description of the size distribution retrieval methodology along with validation is available from *Jumelet et al.* [2008a]. We only recall the most salient features. The particle size distribution is assumed to be lognormal. The size distribution parameters (i.e., particle total number N_o, mean radius r_m, and width σ) are derived from comparisons between simulated and measured backscatter coefficients at 355, 532 and 1064 nm, here MARTHA measurements, using a two-stage procedure. In the first stage, a look-up table of backscatter coefficients is generated using a range of size distribution parameters. The backscatter coefficients are calculated with the microphysical and optical module described previously in section 2.2, assuming again that the aerosol phase is in thermodynamical equilibrium with the gas phase. The required particle refractive index is calculated for the specific environment (pressure, temperature, total HNO_3 and H_2O mixing ratios) corresponding to each measurement point. There is no a priori assumption of the H_2SO_4 mixing ratio, as the current look-up table size distribution actually gives a constraint on the condensed mass H_2SO_4 mixing ratio. As the PSC particles considered in this event are most certainly composed or at the very least dominated optically by liquid STS particles, the use of Mie theory [*Bohren and Huffman*, 1983] in the optical calculations is valid.

[23] In the second stage, the most likely (in the least squares sense) PSC size distribution is identified by matching the calculated and measured backscatter coefficients, taking into account the measurement errors. Our statistical approach is well suited for dealing with the strong non-linearities of the function linking the size distribution and the backscatter coefficient [*Jumelet et al.*, 2008a, 2008c]. The control variables in the minimization procedure are (N_o, r_m, σ). The algorithm looks for the most probable solution as in some cases, the sole best match solution (i.e., least squares solution with no measurement errors), may lead to an unrealistic size distribution. As the unrealistic solutions are found on the edge of the resulting three-dimensional solution cluster of points (N_o, r_m, σ) generated from the uncertainties on the lidar measurements, the latter cluster is filtered to discard them before applying the least squares criterion. The most probable solutions are indeed expected to be in the densest part of the solution cluster.

[24] It is finally worth noting that, in the case of bimodal particle size distributions, the algorithm retrieves an optically equivalent mode which is mainly associated with the mode having the strongest lidar backscattered signal, most often the mode associated to the largest particles.

3.3. CALIOP Spaceborne Lidar

[25] The CALIOP lidar on board the CALIPSO platform is a two-wavelength (532 and 1064 nm) lidar. The inclination of the satellite orbit is 98° and its altitude is 705 km, giving an unprecedented spatiotemporal sampling rate for polar studies. On average, on an orbit, over 300,000 lidar profiles are acquired per day at latitudes poleward of 55°, providing a unique data set for studying the occurrence,
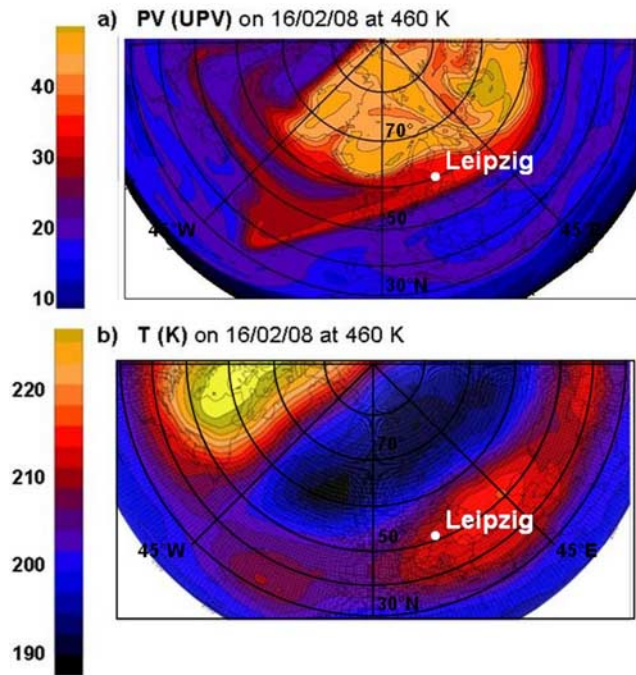
Figure 1. (a) Potential vorticity (PV) and (b) temperature (T) on 16 February 2008 at the 460 K level. PV is calculated from the MIMOSA model, and temperatures come from the ECMWF reanalyses.

composition and evolution of PSCs. CALIOP also separates the 532-nm polarization components [*Winker et al.*, 2007]. The lidar pulse rate is 20.16 Hz, corresponding to a profile every 333 m along the orbit track, and the lidar spot is nearly 80 m in diameter on the Earth's surface. In the PSC altitude range, below 20 km, the horizontal resolution is 1 km and the vertical resolution 60 m. Above this altitude, it decreases to an horizontal resolution of 1.67 km and a vertical resolution of 180 m. Data products are extensively discussed by *Vaughan et al.* [2004]. With a 98° inclination orbit and an altitude of 705 km, CALIPSO has the capabilities to fully investigate PSCs. Nighttime signal-to-noise ratio is about 10 at an altitude of about 25 km when lidar profiles are averaged over 1 km on the vertical and 100 km on the horizontal [*Hunt et al.*, 2009]. The total attenuated backscatter coefficient at 532 nm is normalized to molecular density between 30 and 34 km altitudes. It is expected to be obtained with a bias smaller than 10% in version 2.01 [*Powell et al.*, 2009]. Bias and errors at 1064 nm are expected to be larger by a factor of about 2.

4. Observations

4.1. Meteorological Conditions

[26] During the month of February 2008, the polar vortex experienced several stretches and shifts toward the midlatitudes and northern Europe. In the first days of February, temperatures dropped below 200 K from around the 435 K to 550 K potential temperature levels over northern England. The conditions stayed marginally favorable to PSCs during 2–3 days over this region. Then, the vortex left the area with an eastward rotation accompanied by a local warming,

precluding PSC formation. However, from 16 February, the polar vortex came back above northern Scandinavia. It was substantially distorted with filaments pulling away toward the midlatitudes as displayed in the MIMOSA PV field of Figure 1a. This strong shift toward Europe lasted till around 23 February. Between 17 and 23 February, the temperatures dropped to about 190 K over Europe on the edge of the vortex, around 460 K (see Figures 1b and 2b). The coldest spells were observed during 18 and 19 February. The PSC was detected by the MARTHA ground lidar on the night of 19 and 20 February. At that time, Figure 2a shows that the vortex filament was passing above Leipzig. It was also detected by CALIOP on several overpasses from 17 to 21 February, as the vortex moved (the CALIPSO tracks have been reported in Figure 8). The sharp PV gradients on the edge of the vortex indicate little mixing between polar vortex and the midlatitude air. The coldest area at the time of the lidar measurements is centered between eastern England and western Scandinavia (see Figure 2b) with temperatures remaining around 190 K. These stable PSC conditions during few days could have allowed PSC particles to reach somehow thermodynamical equilibrium and become fully equilibrated PSCs.

4.2. Lidar Data in the IfT Area

[27] Figures 3a and 3c show the multiwavelength particle backscatter coefficient profiles derived from the IfT lidar for two time intervals: 2345–0130 and 0130–0330 UTC. It is worth noting that this PSC event is recorded as one of the highest layer observed at the station. Particles are detected between 18 and around 24 km, with a strongly scattering layer between around 20 and 22 km. Figures 3b and 3d display the associated particle depolarization ratio. Both quantities provide information on the particle type. The high depolarization ratio in the 18.5–19.5 km altitude range of
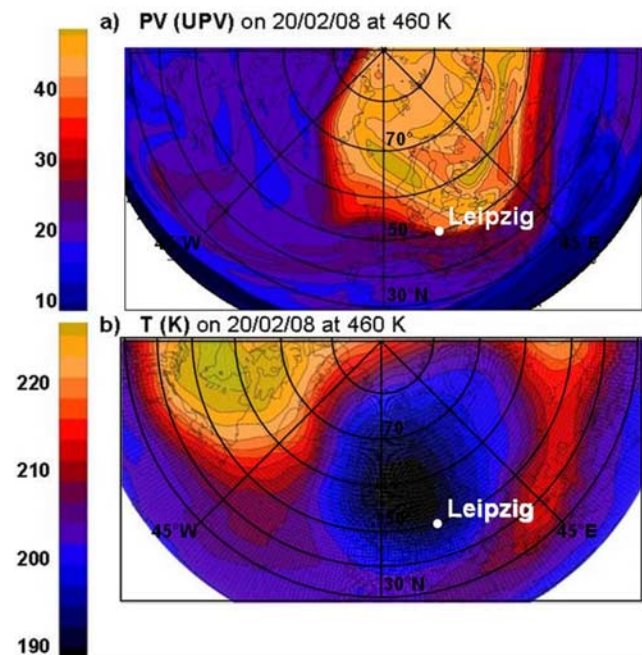

Figure 2. (a) Potential vorticity and (b) temperature on 20 February 2008 at the 460 K level.
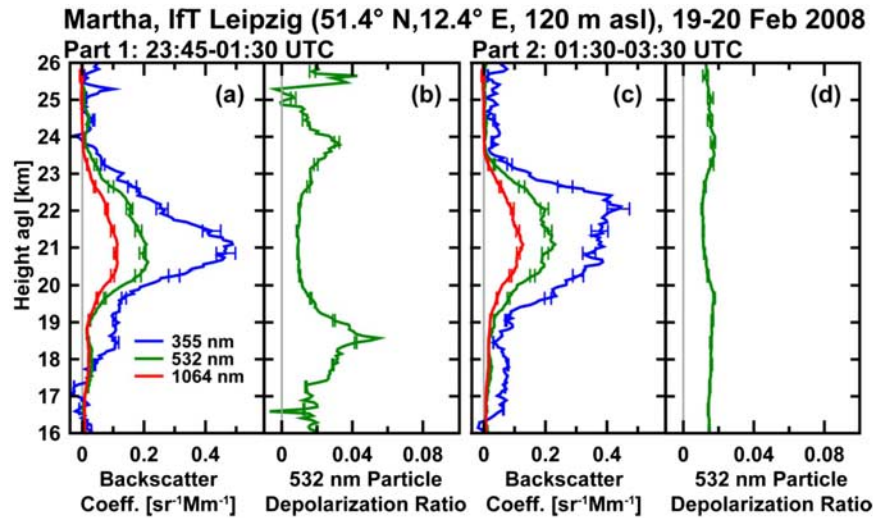
Figure 3. MARTHA lidar measurements performed at the IfT during the night between 19 and 20 February 2008. Two time intervals are considered, around 2345–0130 UTC and 0130–0330 UTC. (a and c) Backscatter coefficient for each time interval. (b and d) Corresponding depolarization. Vertical window smoothing length was 1200 m. Error bars indicate the statistical error.

the first time interval indicate presence of aspherical particles (i.e., solid). Above 19.5 km, the particles are non-depolarizing which is indicative for spherical particles. The lower layer tends to disappear from 0130 UTC. The reason we focus the analysis on the upper layer (around 21 km) is threefold. First, it corresponds to the best signal-to-noise ratio. Second, it is composed of spherical particles (suited to Mie theory; see section 3), and third, its structure is stable throughout the measurement period. Note that the particles in this layer are not necessarily all spherical liquid particles. Solid particles in low number densities may not always be clearly detected on the perpendicular backscatter signal [*Biele et al.*, 2001] and some PSCs detected in the Arctic region are composed of layers having different particle types [*Blum et al.*, 2005].

[28] In the night between 19 and 20 February, the CALIPSO track passed within 30 km from the IfT. This coincidence brings a second and independent source of lidar data to compare to. CALIPSO provides through the vertical slices of the CALIOP instrument an excellent spatial overview of this event. Browsing through the quick looks of the 2.01 version of the CALIPSO backscatter data products (available online at http://www-calipso.larc.nasa.gov/products/ and http://www.icare.lille1-univ.fr/calipso), it appears that the spaceborne lidar started detecting PSCs from 17 February 2008, around 20 km. Between 17 and 20 February the two PSC layers detected by the IfT lidar are identified on the spaceborne lidar profiles, the major one being centered around 21 km, while a lower layer displaying low backscatter and significant depolarization (around 5%) is present between 18 and 20 km.

[29] To be able to carry out quantitative comparisons between the model simulation and the satellite data set, CALIPSO lidar measurements of total attenuated backscatter coefficient have to be normalized to the molecular signal and should be corrected from the particle extinction. The attenuation caused by the PSC layers is however very low (a few percent, that is an extinction coefficient around 0.015 km^{-1}), and, at first order, we will neglect the

attenuation caused by PSC particles. On that case, the attenuated particle backscatter coefficient will be treated as the corrected backscatter. Figure 4 compares backscatter profiles of CALIOP and MARTHA on 20 February at
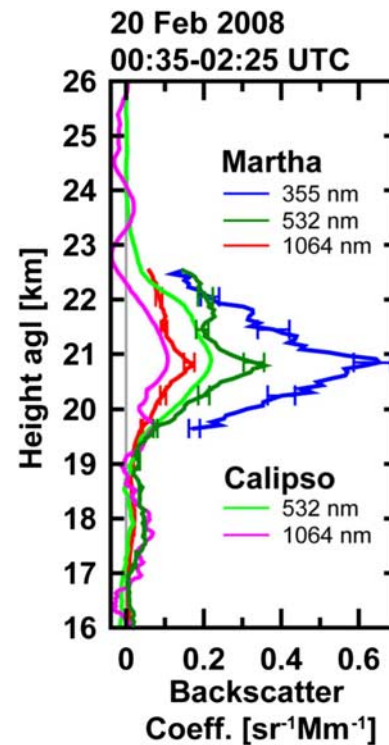

Figure 4. Backscatter profile comparison between the ground-based (MARTHA) and spaceborne (CALIOP/CALIPSO) lidars at 532 and 1064 nm during the overpass on 20 February. CALIPSO overpass at Leipzig was around 0130 UTC. Data between 52.06°N and 50.46°N were averaged. Vertical window smoothing length was 600 m for both instruments. Error bars indicate the statistical error.
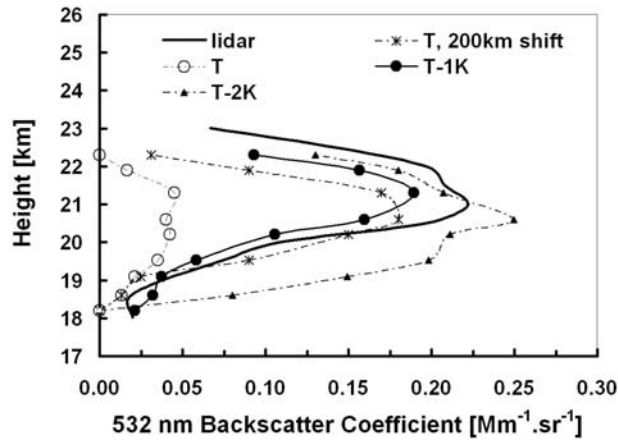
Figure 5. Backscatter profile comparison between the ground-based lidar and the model-simulated optical properties, for the (T), (T-1K), and (T-2K) simulations (see section 2.4), on 20 February 2008, 0000 UTC. Also plotted is a backscatter profile for the MIMOSA-$\mu\varphi$ backscatter, 200 km north of Leipzig.

nighttime. In view of the uncertainties in the lidar data analyses, there is a very good agreement on the PSC vertical structure both at the 532 and 1064 nm wavelengths. The fact that the spaceborne backscatters are slightly lower than the ground-based ones could be due to the uncorrected particle attenuation on the CALIOP signal. Nonetheless, CALIPSO remains the ideal support to local lidar measurements and can be used to characterize the horizontal structures of PSCs at the regional scale, as we will show later.

5. Model Simulations

5.1. Vertical Profiles

[30] Figure 5 shows the profiles of backscatter coefficient for the reference IfT lidar measurements, during the night between 19 and 20 February, together with the profiles calculated above Leipzig by our model MIMOSA-$\mu\varphi$ for the three previously defined simulations: (T), (T-1K) and

(T-2K). The simulation with original ECMWF temperature fails to reproduce the lidar PSC backscatter above 19 km. It might be tempting to attribute this failure to the model resolution, $1° \times 1°$ (i.e., around 255 km). Figure 5 thus also features the backscatter profile calculated 200 km north of Leipzig, in the air mass incoming direction. This 200-km-shifted profile slightly improves the quality of the comparison. As the temperature field is not uniform, a spatial shift is also a temperature shift. A bias in the temperature is certainly possible. It is supported by a slight discrepancy between the ECMWF temperature and a radio-sounding performed at the time of the measurements (20 February, 0000 UTC) at Meiningen (around 200 km from Leipzig). Averaging over the STS PSC altitude range (20–22 km), this comparison reveals a small temperature difference of 0.5 to 1 K. The simulation with a 1 K cold adjustment (T-1K) drastically improves the correlation with the lidar measurements (see Figure 5). The vertical structure is well reproduced. In view of the possible errors in the PSC modeling and its input data, the agreement between the lidar and (T-1K) simulation backscatter profiles is very satisfactory. The (T-2K) simulation displays stronger backscatter coefficients with a poor correlation to the lidar measurements; the vertical structure is not matching the structure of the lidar measurements anymore.

[31] The (T-1K) simulation will thereafter be the only one considered when comparing the lidar-derived and model-simulated geometrical parameters. We will now focus on the large-scale structure, as hinted by the patch of cold temperatures appearing on Figures 1b and 2b.

5.2. Two-Dimensional Isentropic Fields

[32] We have seen in section 5.1 that CALIPSO reported continuous PSC detection from 16 to 23 February. Around 18 February, the CALIOP BR_{532nm} peaks around 4.0 during the coldest period. In the CALIOP data calibration procedure, it is worth mentioning that a high number of profiles is required to get rid of the possible presence of noisy data in the calibration altitude range (typically above 30 km). A maximal 10% residual error is thus expected on absolute values of (BR-1). Figure 6a displays CALIOP BR_{532nm} from 17 to 21 February, on the 468 K potential temperature
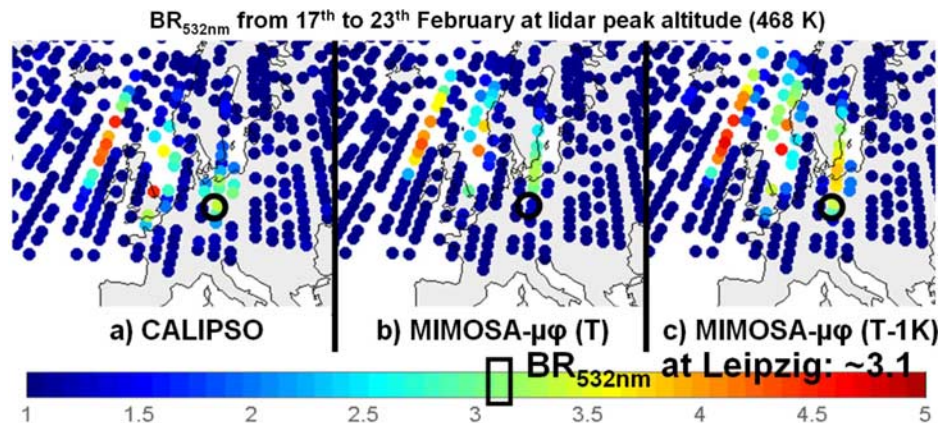

Figure 6. Isentropic backscatter ratio fields (a) as seen by CALIOP, and as calculated by the model for the (b) (T) and (c) (T-1K) simulations from 17 to 23 February 2008. The spaceborne measurements are interpolated on the model output grid, one point every 6 h.
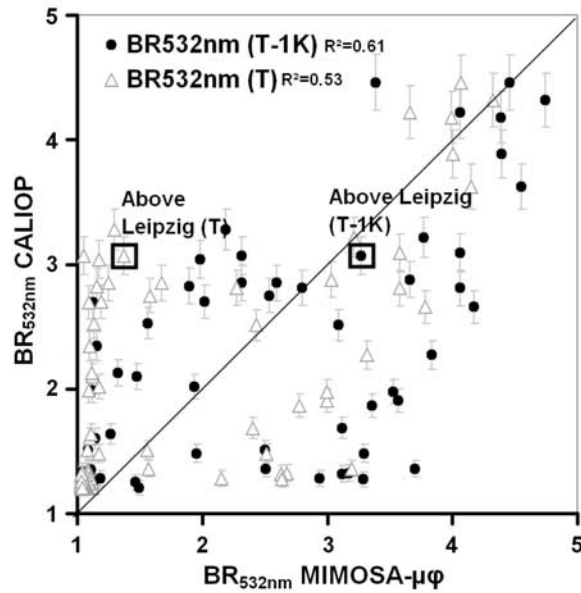
Figure 7. Correlation plot between the CALIOP and MIMOSA-$\mu\varphi$ backscatter ratios using points of Figure 6. Every point at which CALIOP BR_{532nm} is lower than 1.20 is discarded.

level, which corresponds to the lidar backscatter peak altitude. Figures 6b and 6c show the corresponding BR_{532nm} for the (T) and (T-1K) simulation, respectively. The model-simulated BR_{532nm} have been interpolated to the time and position of the CALIOP measurements shown in Figure 6a. The value of IfT BR_{532nm} at the time of the satellite overpass (on 20 of February around 0000 UTC) is also indicated on the colorbar BR scale and is quite consistent with the value we determine from CALIOP above the area, both values being between 3.0 and 3.2. Overall, among the three model simulations, the (T-1K) simulation seems to reproduce best the CALIOP BR field over northern Europe.

[33] A correlation plot between model-simulated and lidar-measured BRs for the (T) and (T-1K) simulations is plotted on Figure 7. Backscatter ratios higher than 1.20 are not included in the correlation analysis in order to make sure that no PSC-free measurements are considered. The results of the (T-2K) simulation are not shown in Figure 7 because the match with the measurements is very poor with most of the points lying in the bottom right-hand corner.

[34] Globally, the correlation coefficient ($R^2 = 0.61$) is the highest for the (T-1K) simulation. Above Leipzig, the CALIOP BR_{532nm} ($\sim$3.0) is well reproduced in the (T-1K) simulation ($BR_{532nm} \sim 3.3$) whereas it is vastly underestimated in the (T) simulation ($BR_{532nm} \sim 1.4$). These relatively high BR values once again confirm presence of liquid STS particles, as NAT particles do not exhibit backscatter ratios higher than 2 typically [*Browell et al.*, 1990; *David et al.*, 1998]. The large spread in the correlation plot clearly shows that the excellent match between the (T-1K) simulation and measurements for the IfT data point is largely fortuitous. The main deficiency in the (T) simulation is the large fraction of data points lying along the CALIOP BR vertical axis indicating observed PSCs that are not present in the simulation. Even if the (T-1K) simulation displays the higher correlation coefficient, the model tends

to overestimate the CALIOP measurements by about 40% on average, especially on the northern part of the domain, on the left of northern Scandinavia. There are several possible reasons for this discrepancy ranging from the neglected particle attenuation when calculating the CALIOP BR_{532nm} to errors on satellite backscatter coefficients (unlikely to be lower than 10%), and to an overestimation of the assumed ECMWF temperature bias. This point is also connected to the spatial scales in Arctic PSC fields, and to the uncertainties in the PSC scheme parameterizations and model input data (thermodynamical data, H_2O, HNO_3, temperature, etc.), and in the model spatial resolution (255 km horizontally) with respect to CALIOP resolution (1 km).

[35] As the (T-1K) simulation is the most able to reproduce the BR magnitude of the IfT measurement and the spatial extension and structures seen in the CALIOP measurements, it is used to illustrate the spatiotemporal evolution of the BR. Figure 8 shows the backscatter ratio fields at various times from 16 to 21 February at 468 K level for the (T-1K) simulation. According to the model results, the PSC started forming on 16 February over the North Atlantic, west of Iceland. Then, the PSC area grew to cover the entire northern Europe including Iceland, Scandinavia and the northern France and Germany. The PSC started fading on 21 of February. The panels illustrate clearly that the IfT lidar did not probe the PSC in the coldest area, which lays a few
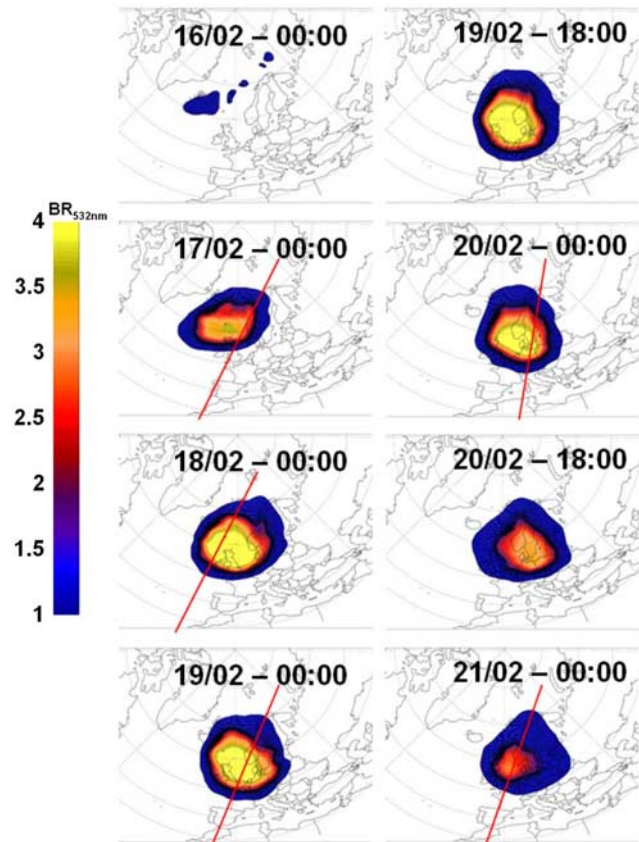

Figure 8. Model-simulated isentropic fields of backscatter ratios from 16 to 21 February 2008 at the 468 K level. Some CALIPSO overpasses (closest to the corresponding output time, typically around 0130–0200 UTC) are also reported.
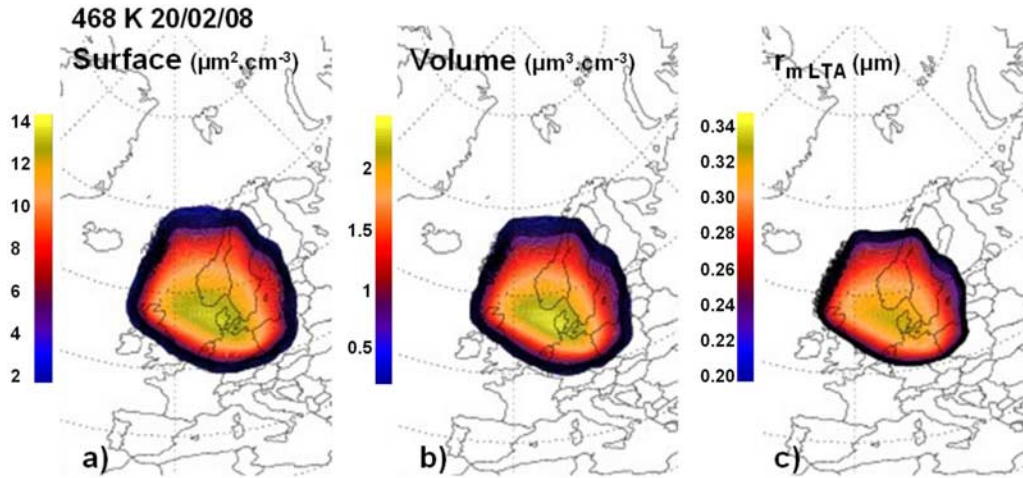
Figure 9. Model-simulated isentropic fields of (a) surface area density (μm^2 cm^{-3}) and (b) volume (μm^3 cm^{-3}), and (c) median radius of the STS particle size distribution (μm), on 20 February 2008, 0000 UTC.

hundred kilometers north, between England and Norway. As expected, the spatiotemporal structure of the model-simulated PSC remains always consistent with the associated temperature structure (not shown), in that the strongest backscatter ratios are observed in the coldest areas.

6. Microphysical Properties

[36] In section 5, the model-simulated optical properties have been compared to ground-based and spaceborne lidar measurements. As the overall agreement is satisfactory, we can now focus on the PSC geometrical properties. In the model, the backscatter ratio is calculated using the particle size distribution which is explicitly resolved with bins. In terms of geometrical properties, it is also possible to calculate the moments of the model-simulated size distribution or derive the three parameters (N_o, r_m, σ) of an equivalent lognormal size distribution. The three parameters can also be retrieved from the IfT multiwavelength lidar measurements (see section 3.2).

6.1. Integrated Size Distribution Properties

[37] The PSC surface area density (A) and volume density (V) are important variables because they determine the rates of processes responsible for ozone depletion. Figures 9a and 9b display A and V fields on 20 February at 0000 UTC, the approximate time of IfT measurements. The particle mean radius is also plotted in Figure 9c. As expected, the structures in A, V and r_m are very similar. The temperature being the critical parameter in PSC formation, A, V and r_m fields reflect the structures in the temperature field (shown in Figure 2b). There is also a good match with the BR_{532nm} field (shown in the 20/02 00:00 UTC image in Figure 8). It is not surprising because the lidar backscatter is mostly sensitive to the higher-order moments of the PSC size distribution such as A. This high sensitivity to the higher-order moments explained why lidar measurements are not very sensitive to the PSC number concentration [*Jumelet et al.*, 2008c], resulting in uncertainties when trying to retrieve this variable [*Jumelet et al.*, 2008a]. Above Leipzig, the model predicts a mean particle radius r_m of about 0.28 μm

at the time of the lidar session at 21 km, in the densest part of the cloud. This r_m value is typical of STS PSCs observed in polar regions [*Deshler et al.*, 2000; *Blum et al.*, 2006]. The high surface area density (around 10 μm^2 cm^{-3}) and volume density (around 1 μm^3 cm^{-3}) for temperatures slightly below 190 K would certainly have had an impact on ozone chemistry through the heterogeneous activation of halogen reservoirs on the PSC surfaces. In contrast to what happens when PSC form in polar regions during winter, midlatitude air masses are always exposed to sunlight. Thus, in these midlatitude air masses, chlorine activation through heterogeneous reactions on PSC particles leads to immediate ozone destruction [*Keckhut et al.*, 2007]. It is interesting to note that such A and V fields may be used to constrain the chemistry-transport models simulating ozone depletion, and therefore validating these fields is a necessary step toward more reliable ozone predictions. However, as seen before the sensitivity of PSC formation on temperature, may require very accurate temperature field analyses.

6.2. Size Distribution Parameters Above Leipzig

[38] The IfT lidar measurements reported in Figure 3 are used to derive the particle size distribution using the methodology described in section 3. The focus is on the particles located around 21 km, previously identified as STS particles. PSC size distributions are retrieved over two time intervals (2345–0130 and 0:30–0333 UTC). Lidar uncertainties on the backscatter coefficient are estimated to be about 15% for the 355 and 532 nm wavelengths and increased to 25% for the 1064 nm, which displays larger uncertainties (see Figure 3). The parameter range of the look-up table for the size distribution retrieval is as follows: $0.01 < N_o < 30$ cm^{-3}, $0.01 < r_m < 1.5$ μm and $1.01 < \sigma < 2.0$. The influence of the look-up table resolution on the retrieval results is checked and increased till such influence is not noticeable [*Jumelet et al.*, 2008a]. To check the consistency and stability of the size distribution retrieval, three different altitudes (20.5, 21 and 21.5 km) are considered. They are centered at the BR peak altitude, 21 km.

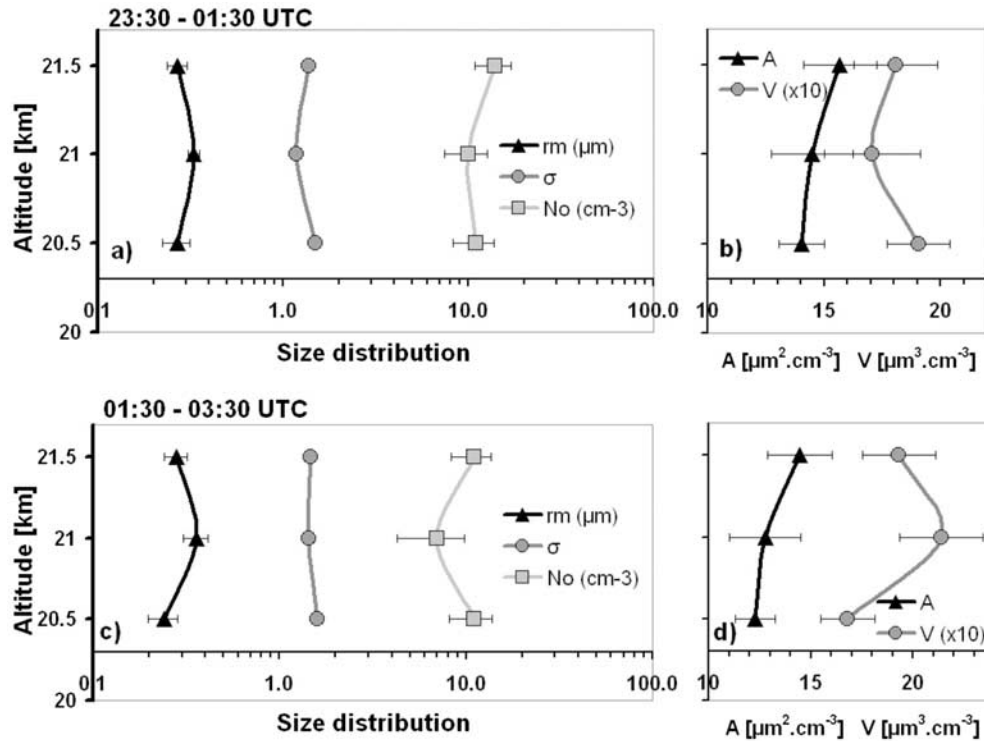[39] Figures 10a and 10c show the retrieved N_o, r_m and σ parameters for the two time intervals whereas Figures 10b

Figure 10. (a and c) Lidar-derived size distribution parameters (N_o, r_m, σ) and (b and d) surface area density (A) and volume (V) for the 2330−0130 UTC (Figures 10a and 10b) and 0130−0330 UTC (Figures 10c and 10d) time intervals on 20 February 2008.

and 10d present the associated particle surface area and volume densities. The results show relatively little variability from one time interval to the next over the 1-km layer. This is expected because the lidar backscatter coefficients around the peak are comparable during the two time intervals. The fact that the PSC size distributions do not vary much with time suggests that conditions are probably favorable to equilibrated particles (i.e., PSC composition in equilibrium with the gas phase). The three altitudes also display comparable size distributions with mean values of $N_o \sim [10{-}15] \, cm^{-3}$, $r_m \sim 0.3 \, \mu m$ and $\sigma \sim 1.50$ over the 1-km layer. The total surface area A is around 14 $\mu m^2 \, cm^{-3}$ and volume V ranges from about 1.7 to 2.0 $\mu m^3 \, cm^{-3}$. The variability on retrieved V is higher than on A because V is more sensitive to fluctuations on r_m and σ than A. A and V have the same sensitivity to fluctuations in N_o. Overall, the retrieved size distributions are consistent with balloon-borne measurements of Arctic PSCs [*Deshler et al.*, 2003] and clearly confirm the STS characterization.

[40] The agreement between lidar-retrieved and model-calculated median radius is excellent with both values being in the 0.28–0.30 μm range. As rates of heterogeneous chemistry and sedimentation depend on powers of r_m, it is important to reproduce accurately this quantity in model simulations. The lidar-retrieved A and V for the two time intervals are averaged on Figure 11 and compared to the results of (T-1K) model simulations carried out at the three considered altitudes. Figure 11 provides three different pairs of A and V: one corresponds to the lidar retrieval, another one is calculated by the MIMOSA-$\mu\varphi$ model (labeled "PSC"), and the last one is also calculated by the model, but for background aerosol levels (labeled "aer" and

calculated by averaging 2 days of model simulations above Leipzig before PSC detection). The increases in A and V caused by PSC formation are of about 1 order of magnitude. The model underestimates the lidar-derived values by about 50% on V and about a factor 2 on A on average. The differences are less pronounced at 21 km, the PSC BR peak, with model-simulated values of around 10 $\mu m^2 \, cm^{-3}$ for A and 1 $\mu m^3 \, cm^{-3}$ for V. The 50% difference in V is intriguing because the total HNO_3 and H_2O masses in the simulation are constrained by the relatively accurate MLS measurements. Once PSCs are formed, almost all the HNO_3 end up in the condensed phase of the HNO_3-rich PSCs, as simulated in the model. Therefore, V is a good indicator of the total HNO_3. Instead of blaming MLS data, the reason for the difference in A and V may lie in biases in the lidar-derived
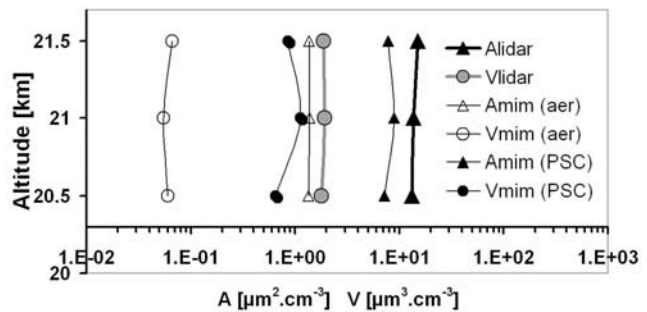

Figure 11. Comparison between the lidar-derived ("lidar") and model-simulated ("mim") particle surface area density and volume density. Background aerosol values calculated by MIMOSA-$\mu\varphi$ are also plotted ("aer").

PSC size distributions. Interestingly, a thorough evaluation of the retrieval results against reference balloon-borne measurements of STS PSC size distributions has showed that, although r_m and σ are reliably retrieved, N_o tended to be overestimated by about 30% [*Jumelet et al.*, 2008a]. When compared to backscatter-derived refractive indices [*Deshler et al.*, 2000], the retrieval of model-simulated refractive index was found to exhibit a small negative bias of 0.03. By increasing the refractive index of the same amount in the retrieval, the algorithm was able to correctly infer the size distribution parameters including N_o [*Jumelet et al.*, 2008a]. Such a small increment on the refractive index is enough to cause a substantial reduction in the retrieved N_o and hence in the surface and volume density, as the refractive index appears to be the most sensitive parameter involved in calculations of the backscatter coefficient [*Jumelet et al.*, 2008c]. Applying the same shift on the refractive index for processing the IfT data would decrease the lidar-derived values of A and V by approximately 30%, bringing them more in line with the model-simulated values. Overall, considering the uncertainties on lidar-derived size distribution parameters and the model inputs such as the temperature, the agreement between the model-derived and geometrical properties is rather satisfactory.

7. Concluding Remarks

[41] The present work is a modeling study of a rare polar stratospheric cloud event observed at northern midlatitudes during February 2008. Ground-based lidar measurements at IfT (Leipzig) and spaceborne lidar measurements CALIOP/CALIPSO indicate that the PSC is mostly composed of STS particles. The event is simulated using a high-resolution microphysics-transport model MIMOSA-$\mu\varphi$ coupled to an optical module that calculates the particle optical properties from the model outputs. Although the microphysical parameterizations are vastly simplified, the model appears to be able to reproduce most of the spatiotemporal structures seen in the time-evolving field of the lidar backscatter measurements. However, to do so, the analyzed temperatures that are used to force the model have to be reduced by about 1 K. With this setup, the model is also able to simulate PSC geometrical properties, as derived from IfT multiwavelength lidar, especially when a correction in the refractive index is specified in the lidar size distribution retrieval algorithm. This temperature correction is partly supported by a radiosounding performed at the time of the lidar measurements in the vicinity of Leipzig, indicating a difference of 0.5 to 1 K over the PSC altitude range (20–22 km). However, this temperature correction is much too small to conclude unambiguously that the ECMWF temperatures are actually biased by 1 K, especially over a large area. Actually, there are larger sources of errors in the model itself [*Carslaw et al.*, 1997]. Overall the results demonstrate the usefulness of the CALIOP satellite data and of ground-based multiwavelength lidar data for PSC studies and for the evaluation of PSC fields simulated in chemistry-transport models. As the particle surface and volume densities of PSCs are the key microphysical parameters for ozone depletion, the validation of models should focus on these quantities when possible. The results of the comparisons between simulations and the lidar data are encouraging, mostly validating the new microphysical-transport model. However, they also confirm the importance of accurate temperature forcings when PSC conditions are marginal, which is often the case in the Arctic. Under those conditions, the results confirm that the prediction of the future evolution of Arctic ozone remains entirely dependent on the quality of the temperature prediction.

References

Adriani, A., P. Massoli, G. Di Donfrancesco, F. Cairo, M. L. Moriconi, and M. Snels (2004), Climatology of polar stratospheric clouds based on lidar observations from 1993 to 2001 over McMurdo Station, Antarctica, *J. Geophys. Res.*, *109*, D24211, doi:10.1029/2004JD004800.

Barnes, J. E., T. Kaplan, H. Vomel, and W. G. Read (2008), NASA/AURA/Microwave Limb Sounder water vapor validation at Mauna Loa Observatory by Raman lidar, *J. Geophys. Res.*, *113*, D15S03, doi:10.1029/2007JD008842.

Ansmann, A., M. Riebesell, and C. Weitkamp (1990), Measurement of atmospheric aerosol extinction profiles with a Raman lidar, *Opt. Lett.*, *15*, 746–748.

Ansmann, A., M. Riebesell, U. Wandinger, C. Weitkamp, E. Voss, W. Lahmann, and W. Michaelis (1992a), Combined Raman elastic-backscatter lidar for vertical profiling of moisture, aerosol extinction, backscatter, and lidar ratio, *Appl. Phys. B*, *55*, 18–28.

Ansmann, A., U. Wandinger, M. Riebesell, C. Weitkamp, and W. Michaelis (1992b), Independent measurement of extinction and backscatter profiles in cirrus clouds by using a combined Raman elastic-backscatter lidar, *Appl. Opt.*, *31*, 7113–7131.

Biele, J., A. Tsias, B. P. Luo, K. S. Carslaw, R. Neuber, G. Beyerle, and T. Peter (2001), Nonequilibrium coexistence of solid and liquid particles in Arctic stratospheric clouds, *J. Geophys. Res.*, *106*(D19), 22,991–23,007, doi:10.1029/2001JD900188.

Blum, U., K. H. Fricke, K. P. Müller, J. Siebert, and G. Baumgarten (2005), Long-term lidar observations of polar stratospheric clouds at Esrange in northern Sweden, *Tellus, Ser. B*, *57*(5), 412–422, doi:10.1111/j.1600-0889.2005.00161.x.

Blum, U., F. Khosrawi, G. Baumgarten, K. Stebel, R. Müller, and K. H. Fricke (2006), Simultaneous lidar observations of a polar stratospheric cloud on the east and west sides of the Scandinavian mountains and microphysical box model simulations, *Ann. Geophys.*, *24*(762), 3267–3277.

Bohren, C. F., and D. R. Huffman (1983), *Absorption and Scattering of Light by Small Particles*, 530 pp., John Wiley, Hoboken, N. J.

Brooks, S. D., O. B. Toon, M. A. Tolbert, D. Baumgardner, B. W. Gandrud, E. V. Browell, H. Flentje, and J. C. Wilson (2004), Polar stratospheric clouds during SOLVE/THESEO: Comparison of lidar observations with in situ measurements, *J. Geophys. Res.*, *109*, D02212, doi:10.1029/2003JD003463.

Browell, E. V., C. F. Butler, S. Ismail, P. A. Robinette, A. F. Carter, N. S. Higdon, O. B. Toon, M. R. Schoeberl, and A. F. Tuck (1990), Airborne lidar observations in the wintertime Arctic stratosphere: Polar stratospheric clouds, *Geophys. Res. Lett.*, *17*(4), 385–388, doi:10.1029/GL017i004p00385.

Carslaw, K. S., B. P. Luo, S. L. Clegg, T. Peter, P. Brimblecombe, and P. J. Crutzen (1994), Stratospheric aerosol growth and HNO_3 and water uptake by liquid particles, *Geophys. Res. Lett.*, *21*(23), 2479–2482, doi:10.1029/94GL02799.

Carslaw, K. S., T. Peter, and R. Muller (1997), Uncertainties in reactive uptake coefficients for solid stratospheric particles: 2. Effect on ozone depletion, *Geophys. Res. Lett.*, *24*(14), 1747–1750, doi:10.1029/97GL01684.

Carslaw, K. S., et al. (1998), Increased stratospheric ozone depletion due to mountain-induced atmospheric waves, *Nature*, *391*, 675–678, doi:10.1038/35589.

Carslaw, K. S., J. A. Kettleborough, M. J. Northway, S. Davies, R. Gao, D. W. Fahey, D. G. Baumgardner, M. P. Chipperfield, and A. Kleinböhl (2002), A vortex-scale simulation of the growth and sedimentation of large nitric acid hydrate particles, *J. Geophys. Res.*, *107*(D20), 8300, doi:10.1029/2001JD000467.

Daerden, F., N. Larsen, S. Chabrillat, Q. Errera, S. Bonjean, D. Fonteyn, K. Hoppel, and M. Fromm (2007), A 3D-CTM with detailed online PSC-microphysics: Analysis of the Antarctic winter 2003 by comparison with satellite observations, *Atmos. Chem. Phys.*, *7*, 1755–1772.

Daneva, D., and T. Shibata (2003), The mixing state of polar stratospheric cloud particles in "sandwich structure" observed by lidar: 2. Numerical simulations of the optical properties of liquid and solid particles with external mixture of STS and NAT particles, *J. Meteorol. Soc. Jpn.*, 81(4), 759–777, doi:10.2151/jmsj.81.759.

David, C., S. Bekki, S. Godin, and G. Mégie (1998), Polar stratospheric clouds climatology over Dumont D'Urville between 1989 and 1993 and the influence of volcanic aerosols on their formation, *J. Geophys. Res.*, 103(D17), 22,163–22,180, doi:10.1029/98JD01692.

David, C., S. Bekki, N. Berdunov, M. Marchand, and G. Mégie (2005), Classification and scales of Antarctic Polar Stratospheric Clouds using wavelet decomposition, *J. Atmos. Sol. Terr. Phys.*, 67, 293–300.

Deshler, T., B. Nardi, A. Adriani, F. Cairo, G. Hansen, F. Fierli, A. Hauchecorne, and L. Pulvirenti (2000), Determining the index of refraction of polar stratospheric clouds above Andoya (69°N) by combing size-resolved concentration and optical scattering measurements, *J. Geophys. Res.*, 105(D3), 3943–3953, doi:10.1029/1999JD900469.

Deshler, T., M. E. Hervig, D. J. Hofmann, J. M. Rosen, and J. B. Liley (2003), Thirty years of in situ stratospheric aerosol size distribution measurements from Laramie, Wyoming (41°N) using balloon-borne instruments, *J. Geophys. Res.*, 108(D5), 4167, doi:10.1029/2002JD002514.

Deshler, T., R. Anderson-Sprecher, H. Jager, J. Barnes, D. J. Hofmann, B. Clemesha, D. Simonich, R. G. Grainger, and S. Godin Beekmann (2006), Trends in the nonvolcanic component of stratospheric aerosol over the period, *J. Geophys. Res.*, 111, D01201, doi:10.1029/2005JD006089.

Eckermann, S. D., A. Dornbrack, S. B. Vosper, H. Flentje, M. J. Mahoney, T. P. Bui, and K. S. Carslaw (2006), Mountain wave-induced polar stratospheric cloud forecasts for aircraft science flights during SOLVE/THESEO 2000, *Weather Forecast.*, 21(1), 42–68, doi:10.1175/WAF901.1.

Engel, A., C. Schiller, U. Schmidt, R. Borchers, H. Ovarlez, and J. Ovarlez (1996), The total hydrogen budget in the Arctic winter stratosphere during the European Arctic Stratospheric Ozone Experiment, *J. Geophys. Res.*, 101(D9), 14,495–14,503, doi:10.1029/95JD03766.

Fromm, M. D., J. D. Lumpe, R. M. Bevilacqua, E. P. Shettle, J. Hornstein, S. T. Massie, and K. H. Fricke (1997), Observations of Antarctic polar stratospheric clouds by POAM II: 1994–1996, *J. Geophys. Res.*, 102(D19), 23,659–23,672, doi:10.1029/97JD00794.

Fromm, M. D., J. Alfred, and M. Pitts (2003), A unified, long-term, high-latitude stratospheric aerosol and cloud database using SAM II, SAGE II, and POAM II/III data: Algorithm description, database definition, and climatology, *J. Geophys. Res.*, 108(D12), 4366, doi:10.1029/2002JD002772.

Fueglistaler, S., S. Buss, B. P. Luo, H. Wernli, C. A. Hostetler, L. R. Poole, K. S. Carslaw, and T. Peter (2003), Detailed modeling of mountain wave PSC, *Atmos. Chem. Phys. Discuss.*, 3, 253–299.

Goodman, J., O. B. Toon, R. F. Pueschel, K. G. Snetsinger, and S. Verma (1989), Antarctic stratospheric ice clouds, *J. Geophys. Res.*, 94(D14), 16,449–16,458, doi:10.1029/JD094iD14p16449.

Hansen, G., and U. P. Hoppe (1997), Lidar observations of polar stratospheric clouds and stratospheric temperature in winter 1995/96 over Northern Norway, *Geophys. Res. Lett.*, 24(2), 131–134, doi:10.1029/96GL03796.

Hanson, D., and K. Mauersberger (1988), Laboratory studies of the nitric acid trihydrate: Implications for the south polar stratosphere, *Geophys. Res. Lett.*, 15(8), 855–858, doi:10.1029/GL015i008p00855.

Hauchecorne, A., S. Godin, M. Marchand, B. Heese, and C. Souprayen (2002), Quantification of the transport of chemical constituents from the polar vortex to midlatitudes in the lower stratosphere using the high-resolution advection model MIMOSA and effective diffusivity, *J. Geophys. Res.*, 107(D20), 8289, doi:10.1029/2001JD000491.

Heese, B., S. Godin, and A. Hauchecorne (2001), Forecast and simulation of stratospheric ozone filaments: A validation of a high-resolution PV advection model by airborne ozone lidar measurements in winter 1998–1999, *J. Geophys. Res.*, 106(17), 20,011–20,024, doi:10.1029/2000JD900818.

Hendricks, J., F. Baier, G. Günther, B. C. Krüger, and A. Ebel (2001), Stratospheric ozone depletion during the 1995–1996 Arctic winter: 3-D simulations on the potential role of different PSC types, *Ann. Geophys.*, 19(9), 1163–1181.

Hunt, W., D. M. Winker, M. A. Vaughan, K. A. Powell, P. L. Lucker, and C. Weimer (2009), CALIPSO lidar description and performance assessment, *J. Atmos. Oceanic Technol.*, doi:10.1175/2009JTECHA1223.1, in press.

Irie, H., M. Koike, Y. Kondo, G. E. Bodecker, M. Y. Danilin, and Y. Sasano (2001), Redistribution of nitric acid in the Arctic lower stratosphere during the winter of 1996–1997, *J. Geophys. Res.*, 106(D19), 23,139–23,150, doi:10.1029/2001JD900240.

Jumelet, J., S. Bekki, C. David, and P. Keckhut (2008a), Statistical estimation of stratospheric particle size distribution by combining optical modeling and lidar scattering measurements, *Atmos. Chem. Phys.*, 8, 5435–5448.

(Available at http://www.atmos-chem-phys.net/8/5435/2008/acp-8-5435-2008.html)

Jumelet, J., S. Bekki, C. David, P. Keckhut, and G. Baumgarten (2008b), Size distribution time series of a polar stratospheric cloud event observed above Arctic Lidar Observatory for Middle Atmosphere Research (ALOMAR) (69°N) and analyzed from multiwavelength lidar measurements during the winter 2005, *J. Geophys. Res.*, 114, D02202, doi:10.1029/2008JD010119.

Jumelet, J., C. David, S. Bekki, and P. Keckhut (2008c), Uniwavelength lidar sensitivity to spherical aerosol microphysical properties for the interpretation of Lagrangian stratospheric observations, *J. Atmos. Sol. Terr. Phys.*, 71, 121–131, doi:10.1016/j.jastp.2008.09.038.

Keckhut, P., C. David, M. Marchand, S. Bekki, J. Jumelet, A. Hauchecorne, and M. Hopfner (2007), Observation of polar stratospheric clouds down to the Mediterranean coast, *Atmos. Chem. Phys.*, 7, 5275–5281.

Knudsen, B. M. (1996), Accuracy of arctic stratospheric temperature analyses and the implications for the prediction of polar stratospheric clouds, *Geophys. Res. Lett.*, 23(25), 3747–3750, doi:10.1029/96GL03541.

Knudsen, B. M., J. P. Pommereau, A. Garnier, M. Nunes-Pinharanda, L. Denis, P. Newman, G. Letrenne, and M. Durand (2002), Accuracy of analyzed stratospheric temperatures in the winter Arctic vortex from infrared Montgolfier long-duration balloon flights: 2. Results, *J. Geophys. Res.*, 107(D20), 4316, doi:10.1029/2001JD001329.

Krieger, U. K., J. C. Mössinger, B. P. Luo, U. Weers, and T. Peters (2000), Measurements of the refractive indices of $H_2SO_4/HNO_3/H_2O$ solutions to stratospheric temperatures, *Appl. Opt.*, 39(21), 3691–3703, doi:10.1364/AO.39.003691.

Larsen, N. (2000), Polar stratospheric clouds microphysical and optical models, *Sci. Rep. 00–06*, 85 pp., Dan. Meteorol. Inst., Copenhagen.

Larsen, N., et al. (2002), Microphysical mesoscale simulations of polar stratospheric cloud formation constrained by in situ measurements and optical cloud properties, *J. Geophys. Res.*, 107(D20), 8301, doi:10.1029/2001JD000999.

Larsen, N., et al. (2004), Formation of solid particles in synoptic-scale Arctic PSCs in early winter 2002/2003, *Atmos. Chem. Phys.*, 4, 2001–2013.

Lary, D. J., M. P. Chipperfield, J. A. Pyle, W. A. Norton, and L. P. Riishojgaad (1995), Three dimensional tracer initialization and general diagnostics using equivalent PV latitude—Potential temperature coordinates, *Q. J. R. Meteorol. Soc.*, 121, 187–210.

Lefevre, F., L. P. Riishojgaard, D. Cariolle, and P. Simon (1991), Modeling the February 1990 polar stratospheric cloud event and its potential impact on the Northern Hemisphere ozone content, *J. Geophys. Res.*, 96(D12), 22,509–22,534, doi:10.1029/91JD02400.

Luo, B. P., K. S. Carslaw, T. Peter, and S. L. Clegg (1995), Vapour pressures of $H_2SO_4/HNO_3/HCl/HBr/H_2O$ solutions to low stratospheric temperatures, *Geophys. Res. Lett.*, 22(3), 247–250, doi:10.1029/94GL02988.

Luo, B., U. K. Krieger, and T. Peter (1996), Densities and refractive indices of $H_2SO_4/HNO_3/H_2O$ solutions to stratospheric temperatures, *Geophys. Res. Lett.*, 23(25), 3707–3710, doi:10.1029/96GL03581.

Marchand, M., S. Bekki, F. Lefevere, and A. Hauchecorne (2007), Temperature retrieval from stratospheric O_3 and NO_3 GOMOS data, *Geophys. Res. Lett.*, 34, L24809, doi:10.1029/2007GL030280.

Marti, J., and K. Mauersberger (1993), Laboratory simulations of PSC particle formation, *Geophys. Res. Lett.*, 20(5), 359–362, doi:10.1029/93GL00083.

Mattis, I., A. Ansmann, D. Althausen, V. Jaenisch, U. Wandinger, D. Müller, Y. F. Arshinov, S. M. Bobrovnikov, and I. B. Serikov (2002), Relative-humidity profiling in the troposphere with a Raman lidar, *Appl. Opt.*, 41(30), 6451–6462, doi:10.1364/AO.41.006451.

Mattis, I., D. Müller, A. Ansmann, U. Wandinger, J. Preißler, P. Seifert, and M. Tesche (2008), Ten years of multiwavelength Raman lidar observations of free-tropospheric aerosol layers over central Europe: Geometrical properties and annual cycle, *J. Geophys. Res.*, 113, D20202, doi:10.1029/2007JD009636.

McCormick, M. P., P. Hamill, T. J. Pepin, W. P. Chu, T. J. Swissler, and L. R. McMaster (1979), Satellite studies of the stratospheric aerosol, *Bull. Am. Meteorol. Soc.*, 60(9), 1038–1046, doi:10.1175/1520-0477(1979)060<1038:SSOTSA>2.0.CO;2.

Mehrtens, H., U. von Zahn, F. Fierli, B. Nardi, and T. Deshler (1999), Type I PSC-particle properties: Measurements at ALOMAR 1995 to 1997, *Geophys. Res. Lett.*, 26(5), 603–606, doi:10.1029/1999GL900027.

Mote, P. W., K. H. Rosenlof, M. E. McIntyre, E. S. Carr, J. C. Gille, J. R. Holton, J. S. Kinnersly, H. C. Pumphrey, J. M. Russell, and J. W. Waters (1996), An atmospheric tape recorder: The imprint of tropical tropopause temperatures on stratospheric water vapor, *J. Geophys. Res.*, 101(D2), 3989–4006, doi:10.1029/95JD03422.

Mueller, K. J., L. Di Girolamo, M. Fromm, and S. P. Palm (2008), Stereo observations of polar stratospheric clouds, *Geophys. Res. Lett.*, 35, L17813, doi:10.1029/2008GL033792.

Noel, V., A. Hertzog, H. Chepfer, and D. M. Winker (2008), Polar stratospheric clouds over Antarctica from the CALIPSO spaceborne lidar, *J. Geophys. Res.*, 113, D02205, doi:10.1029/2007JD008616.

Palm, S. P., M. Fromm, and J. Spinhirne (2005), Observations of Antarctic polar stratospheric clouds by the Geoscience Laser Altimeter System (GLAS), *Geophys. Res. Lett.*, 32, L22S04, doi:10.1029/2005GL023524.

Pinnick, R. G., J. M. Rosen, and D. J. Hofmann (1976), Stratospheric aerosol measurements III: Optical model calculations, *J. Atmos. Sci.*, 33, 304–314, doi:10.1175/1520-0469(1976)033<0304:SAMIOM>2.0.CO;2.

Pitts, M. C., L. W. Thomason, L. R. Poole, and D. M. Winker (2007), Characterization of polar stratospheric clouds with Spaceborne lidar: CALIPSO and the 2006 Antarctic season, *Atmos. Chem. Phys.*, 7, 5207–5228.

Polyakov, A. V., Y. M. Timofeev, and Y. A. Virolainen (2008), Polar stratospheric clouds from satellite observational data, *Izv. Russ. Acad. Sci. Atmos. Oceanic Phys., Engl. Transl.*, 44(4), 448–458, doi:10.1134/S0001433808040051.

Poole, L. R., and M. P. McCormick (1988), Airborne lidar observations of arctic polar stratospheric clouds—Indications of 2 distinct growth stages, *Geophys. Res. Lett.*, 15(1), 21–23, doi:10.1029/GL015i001p00021.

Poole, L. R., and M. C. Pitts (1994), Polar stratospheric cloud climatology based on stratospheric aerosol measurement: 2. Observations from 1978 to 1989, *J. Geophys. Res.*, 99(D6), 13,083–13,089, doi:10.1029/94JD00411.

Powell, K. A., et al. (2009), CALIPSO lidar calibration algorithms: Part I — Nighttime 532-nm parallel channel and 532-nm perpendicular channel, *J. Atmos. Oceanic Technol.*, doi:10.1175/2009JTECHA1242.1, in press.

Proffitt, M. H., J. J. Margitan, K. K. Kelly, M. Loewenstein, J. R. Podolske, and K. R. Chan (1990), Ozone loss in the Arctic polar vortex inferred from high-altitude aircraft measurements, *Nature*, 347, 31–36, doi:10.1038/347031a0.

Pullen, S., and R. L. Jones (1997), Accuracy of temperatures from UKMO analyses of 1994/95 in the arctic winter stratosphere, *Geophys. Res. Lett.*, 24(8), 845–848, doi:10.1029/97GL00754.

Santee, M. L., A. Tabazadeh, G. L. Manney, M. D. Fromm, R. M. Bevilacqua, J. W. Waters, and E. J. Jensen (2002), A Lagrangian approach to studying Arctic polar stratospheric clouds using UARS MLS HNO$_3$ and POAM II aerosol extinction measurements, *J. Geophys. Res.*, 107(D10), 4098, doi:10.1029/2000JD000227.

Schoeberl, M. R., L. R. Lait, P. A. Newman, and J. E. Rosenfield (1997), The structure of the polar vortex, *J. Geophys. Res.*, 97(D8), 7859–7882.

Solomon, S. (1999), Stratospheric ozone depletion: A review of concepts and history, *Rev. Geophys.*, 37(3), 275–316, doi:10.1029/1999RG900008.

Tabazadeh, A., R. P. Turco, K. Drdla, and M. Z. Jacobson (1994), A study of type I polar stratospheric cloud formation, *Geophys. Res. Lett.*, 21(15), 1619–1622, doi:10.1029/94GL01368.

Toon, O. B., R. P. Turco, D. Westphal, R. Malone, and M. S. Liu (1988), A multidimensional model for aerosols: Description of computational analogs, *J. Atmos. Sci.*, 45, 2123–2143, doi:10.1175/1520-0469(1988)045<2123:AMMFAD>2.0.CO;2.

Toon, O. B., E. V. Browell, S. Kinne, and J. Jordan (1990), An analysis of lidar observations of polar stratospheric clouds, *Geophys. Res. Lett.*, 17(4), 393–396, doi:10.1029/GL017i004p00393.

Turco, R. P., P. Hamill, O. B. Toon, R. C. Whitten, and C. S. Kiang (1979), The NASA-Ames Research Center Stratospheric Aerosol Model, I. Physical processes and computational analogs, *NASA Tech. Pap., 1362*, 94 pp.

Vaughan, M., S. Young, D. M. Winker, K. Powell, A. Omar, Z. Y. Liu, Y. X. Hu, and C. Hostetler (2004), Fully automated analysis of space-based lidar data: An overview of the CALIPSO retrieval algorithms and data products, *Proc. SPIE Int. Soc. Opt. Eng.*, 5575, 16–30.

Voigt, C., et al. (2000), Nitric acid trihydrate (NAT) in polar stratospheric clouds, *Science*, 290, 1756–1758, doi:10.1126/science.290.5497.1756.

Voigt, C., et al. (2005), Nitric acid trihydrate (NAT) formation at low NAT supersaturation in polar stratospheric clouds (PSC), *Atmos. Chem. Phys.*, 5, 1371–1380.

Vomel, H., et al. (2007), Validation of Aura Microwave Limb Sounder water vapor by balloon-borne Cryogenic Frost point Hygrometer measurements, *J. Geophys. Res.*, 112, D24S37, doi:10.1029/2007JD008698.

Weisser, C., K. Mauersberger, J. Schreiner, N. Larsen, F. Cairo, A. Adriani, J. Ovarlez, and T. Deshler (2006), Composition analysis of liquid particles in the Arctic stratosphere under synoptic conditions, *Atmos. Chem. Phys.*, 6, 689–696.

Wetzel, G., et al. (2002), NO$_y$ partitioning and budget and its correlation with N$_2$O in the Arctic vortex and in summer midlatitudes in 1997, *J. Geophys. Res.*, 107(D16), 4280, doi:10.1029/2001JD000916.

Winker, D. M., R. H. Couch, and M. P. McCormick (1996), An overview of LITE: NASA's lidar in-space technology experiment, *Proc. IEEE*, 84(2), 164–180, doi:10.1109/5.482227.

Winker, D. M., C. A. Hostetler, and W. H. Hunt (2003), Cloud-aerosol Lidar with orthogonal polarization (CALIOP), in *IGARSS 2003: IEEE International Geoscience and Remote Sensing Symposium*, pp. 1514–1516, Inst. of Electr. and Electron. Eng., New York.

Winker, D. M., M. Vaughan, and B. Hunt (2006), The CALIPSO mission and initial results, from CALIOP, *Proc. SPIE Int. Soc. Opt. Eng.*, 6409, 40,902–40,902.

Winker, D. M., W. H. Hunt, and M. J. Gill (2007), Initial performance assessment of CALIOP, *Geophys. Res. Lett.*, 34, L19803, doi:10.1029/2007GL030135.

Wirth, M., A. Tsias, A. Dornbrack, V. Weiss, K. S. Carslaw, M. Leutbecher, W. Renger, H. Volkert, and T. Peter (1999), Model-guided Lagrangian observation and simulation of mountain polar stratospheric clouds, *J. Geophys. Res.*, 104(D19), 23,971–23,981, doi:10.1029/1998JD100095.

World Meteorological Organization (WMO) (2006), Assessment of Stratospheric Aerosol Properties (ASAP), *WCRP-124*, 348 pp., Geneva, Switzerland.

World Meteorological Organization (WMO) (2007), Scientific assessment of ozone depletion: 2006, *Global Ozone Res. and Monit. Proj. Rep. 50*, 572 pp., Geneva, Switzerland.

―――――――――――――

S. Bekki, J. Jumelet, N. Montoux, J. Pelon, and J.-P. Vernier, Service d'Aéronomie, IPSL, UPMC, CNRS, 4 place Jussieu, Tour 45-46, F-75252 Paris, France. (slimane.bekki@aero.jussieu.fr; julien.jumelet@aero.jussieu.fr; monn@aerov.jussieu.fr; jacques.pelon@aero.jussieu.fr; jean-paul.vernier@aerov.jussieu.fr)

P. Seifert, Leibniz Institute for Tropospheric Research, Permoserstrasse 15, D-04318 Leipzig, Germany. (seifert@tropos.de)